Effects of Upstream Endwall Film-cooling on a Vane Cascade Flow-field

Gazi I. Mahmood*, Keenesh Arnachellan

Dept. of Mechanical and Aeronautical Engineering, University of Pretoria, South Africa.

*Corresponding author, E-mail: gazi.mahmood@up.ac.za

Abstract

The effects of film-cooling on the endwall region flow and aerodynamic losses are investigated experimentally as the film-flow is delivered from the slots in the endwall upstream of a linear vane cascade. Four slots inclined at 30° deliver the film-jet parallel to the main flow at four blowing ratios between 1.1 and 2.3 and at a temperature ratio of 1.0. The slots are employed in two configurations pitchwise- all four slots open (case-1) and two middle slots open (case-2). The inlet Reynolds number to the cascade is 2.0E+05. Measurements of the blade surface pressure, axial vorticities, yaw angles, and total pressure loss distributions along the cascade are reported with and without (Baseline) the film-cooling flow. The results show the film-flow changes the orientations, distributions, and strength of the endwall secondary flows and boundary layer. The case-1 of film-cooling provides more mass-flux and momentum than the case-2 affecting the passage vortex legs. The overall total pressure losses at the cascade exit are always lower for the film-cooling cases than for the Baseline. The overall losses are also lower at the low blowing ratios, but higher at the high blowing ratios for the film-cooling case-1 than for the case-2.

Keywords: passage vortex, endwall region, pressure side, suction side, secondary losses.

Nomenclature

C, C_{ax}, P, S	=	true blade-chord, axial blade-chord, pitch, span
$C_{P,Blade}$	=	blade surface static pressure coefficient
$C_{pt,loss}$, $C_{Pt,Loss}$	=	total pressure loss coefficient
M	=	passage mass flow rate
MFR, M_{in}	=	mass fraction ratio, inlet blowing ratio
$P_{b,x}$	=	pressure on blade surface
$P_{s,r}$, $P_{t,r}$	=	(static pressure, total pressure) at reference plane
$P_{t,x}$, $P_{t,box}$	=	local total pressure at exit, total pressure in plenum box

PS, SS, TE = pressure-side, suction-side, trailing edge

Re = inlet Reynolds number based on actual-chord

U = freestream velocity

(X, Y, Z) = local Cartesian coordinates

(X_G, Y_G, Z_G) = global Cartesian coordinates

Lower Case

u, v, w = velocity components along (X, Y, Z)

s = blade surface coordinate

Greek

δ = boundary layer thickness

Δ = change in related quantity

ω = vorticity

ρ = density

1. Introduction

Film-cooling of the endwall in the nozzle-vane or rotor passage of the gas turbine is employed to protect the endwall from the hot combustion gas and reduce the thermal stresses on the endwall. Recent investigations in the blade cascades indicate that the film-flow interacts with the boundary layer and flow separation in the endwall region affecting the passage vortex structures and film-coverage on the endwall. The intensities of such interactions depend on the locations and geometry of the coolant supplying holes or slots and mass-flux of the coolant flow. The endwall film-flow thus increases or decreases the secondary flow losses across the blade passage. The aerodynamic measurements in the blade cascade employing the endwall film-cooling flow are necessary to quantify the secondary losses. The results predict the effects of a specific coolant flow configuration on the aerodynamic performance of the nozzle-vane or rotor row in the gas turbine. The present investigation employs discrete slots for the film-cooling flow at the inlet of a linear vane cascade for the aerodynamic measurements. The slots may also represent the clearance gap at the combustor-turbine interface or the gap between the turbine discs or the densely packed coolant holes in the endwall upstream of the blade leading edge.

The evolution and structures of endwall secondary flows and their effects inside a linear blade cascade have been documented thoroughly in the investigations of Wang et al. [1], Simon and Piggush [2], Mahmood et al. [3], and Ligrani et al.[4]. The studies find that the endwall region secondary flows originate at the junction of blade leading

edge and endwall as the horseshoe vortex, then evolve and travel along the passage endwall as the pressure-side leg vortex and suction-side leg vortex, and finally develop into the single passage vortex structure to travel along the blade suction side toward the passage exit. The secondary flow structures increase pressure losses and endwall heat transfer across the blade passage. Thomas and Povey [5], Friedrichs et al. [6], and Salvadori et al. [7] report the aerodynamic losses at the exit of cascade passage due to the film-cooling flow from discrete holes in the endwall. The adverse effects of the secondary flows and configuration of film-cooling holes on the endwall coolant coverage and effectiveness are investigated by Bogard and Thole [8], Mahmood et al. [9] and Li et al. [10, 11].

The investigations of film-cooling in the rotor- or vane-blade cascades employing a continuous slot in the endwall upstream in [12-17] simulate the film-cooling flow supplied through the leakage gap between two platforms and two mounting disks in the gas turbine. The slot injected coolant in Blanco et al. [12] and Papa et al. [13] is delivered from the endwall misaligned with cascade endwall and interacts with the endwall flow increasing the flow losses at the cascade exit. Du and Li [14] also report the effects of slot film-cooling on the endwall and stagnation region flow in the cascade misaligned with the upstream boundary layer platform. The numerical results of [14] include the effects of geometry of the film-cooling slot to indicate the weakening of secondary flows and the good film coverage on endwall when the slot is narrow and the cascade endwall is lower than the upstream platform. The high momentum of the slot film-flow in Oke et al. [15], Thole and Thrift [16], and Erickson and Simon [17] strongly influences the endwall boundary layer and secondary flows when the slot inclination relative to the endwall is small. The investigations of purge flow from the upstream endwall gaps in the cascade in [18-20] show strong interactions of the purge flow with the endwall flow and increase in the secondary losses at the cascade exit. Although the purge flow is not employed as the film-cooling flow, the purge flow and purge gap geometry in the endwall conform to the flow and geometry of the continuous slot film-cooling.

All the past investigations of the film-cooling flow delivered either through the endwall slots or cooling holes are intended to quantify and improve the film-cooling effectiveness on the cascade endwall. The resulting increase or decrease of the secondary flow losses are unintentional but imminent due to the coolant flows. The interactions between the coolant flow and endwall boundary layer also dictate the coolant flow trajectories and coverage on the endwall as well as the near endwall flow field, all of which are very specific of the geometry and configuration of the coolant delivery means. The past investigations have not provided details of the aerodynamics effects of the film-flow from the leading edge slots distinctively. The present efforts enhance the understanding of the interactions between the film-flow from slots and endwall flow-field and are expected to contribute in the optimum configuration of the film-cooling design. The present investigation measures the flow field near the endwall in a

stationary vane cascade employing four discrete slots located pitchwise just upstream of each vane passage. Two of the slots are located upstream of the blade leading edge. The measurements along different pitchwise planes in the passage quantify the endwall region flow field and secondary flow losses.

2. Experimental Setup and Measurement Methods

Figure 1(a) shows a schematic representation of the atmospheric wind tunnel facility that houses the linear cascade test section. The schematic drawing shows the relative positions of different components clearly which are otherwise difficult to identify in a picture of the whole test facility. The tunnel operates in an open circuit as the air flow is generated by the suction of two large duct fans (7.5 kW and 15 kW) connected in series at the exit (not shown in Fig. 1(a)). The tunnel cross-section is rectangular and the walls are made of wood. The test section walls are made of the transparent polycarbonate. A smooth two-dimensional contraction allows the ambient air to accelerate smoothly and flow into the tunnel settling-length section through a set of honeycomb and mesh screens. The cascade test section as shown in Fig. 1(a) houses seven two-dimensional vane-blades numbered as 1 to 7 and attached to the endwalls with screws. The blade geometry is created by extruding the hub-side vane profile of the GE-E^3 first stage nozzle guide vane [21]. The test geometry employs 6 times the geometry of the actual nozzle vane geometry at the hub-side of the GE-E^3 engine. The vane-blades are manufactured from the polycarbonate and coated with polyurethane for a smooth surface finish. Table 1 provides the geometric parameters employed for the cascade test section. The flow incidence angle is set to 0° at the blade leading edge. Some air flow from the upstream settling-length section is by-passed through the sides of the two blades 1 and 7 to create a periodic flow condition in the test section. The shaded region in Fig. 1(a) between the blade 3 and 5 identifies the measurement region. The blades 3, 4, and 5 have pressure tap holes of diameter 0.3 mm located along the profile at the mid-span height. The hollow core of the blades allows the pressure taps to be connected to a pressure transducer with the plastic tubes through a multi-port scanner. The cut-out sections in the top endwall adjacent to the blade tips and the hollow cores inside the blades are used to run out the plastic tubes connected to the pressure taps.

As shown in Fig. 1(a), a passive turbulence grid made up of 6 mm cylindrical rods is placed in the tunnel at $6.5C_{ax}$ upstream of the cascade inlet. A cut-out slot on the top endwall at $2.5C_{ax}$ upstream of the cascade inlet allows the measurements of the reference properties in Table 2. The reference properties are measured using a pitot-static pressure probe, a thermocouple, and a constant temperature hot-wire anemometer. The probes scan the pitchwise normal plane (Reference-plane) of Fig. 1(a) for the reference properties. The freestream velocity and turbulence

in Table 2 are then reported above the boundary layer from the bottom endwall. As the pressure drop across the test facility is low, the air-flow density in Table 2 is assumed constant in the measurements and obtained from the ideal gas law. The Re in the table is estimated based on the freestream velocity at the reference plane and actual blade-chord length, C. Figure 1(b) shows schematically the secondary flow circuit employed to supply the film-cooling flow in the test section bottom endwall. A blower (1 kW) and an axial fan (800 W) in series deliver the film-flow into a plenum-box located underneath the film-cooling slots through two metered-pipes of diameter 10.2 cm and 5.1 cm as shown in Fig. 1(b). The ISO standard orifice plates in the pipes provide the mass flow rate of the film-flow. The temperature of the film-flow is controlled by the evaporator (heat exchanger) of a refrigerant vapor-compression unit just upstream of the plenum. The wooden walls of the plenum are thermally insulated. Also, the large volume of the plenum diffuses the turbulence and velocity in the coolant flow before it enters the film-cooling slots. Static pressure taps located in the plenum walls are connected to a differential pressure transducer and provide measurements of the total pressure of the coolant flow. Equation (1) then estimates the inlet blowing ratio from the measured pressures based on [6]. The blower speed in Fig. 1(b) is varied to control the coolant mass flow rate to the desired inlet blowing ratio.

$$M_{in} = \sqrt{\frac{P_{t,box} - P_{s,r}}{P_{t,r} - P_{s,r}}} \tag{1}$$

In the measurement region between the blades 3 and 5, three cut-out slots on the top endwall facilitate the flow measurements with a five-hole pressure probe. The location and orientation of the slots are shown in Fig. 2(a) by plane-1 to plane-3. The plane-1 is perpendicular to the blade suction side, while the plane-2 and plane-3 are the pitchwise normal planes. The local (X, Y, Z) and global (X_G, Y_G, Z_G) coordinate systems employed in the measurements are also indicated in Fig. 2(a). The origin of (X_G, Y_G, Z_G) is located at the leading edge of blade 4. The local coordinates (X, Y, Z) originate from the suction-side of blade 4. The location (Y_G or Y=0) then refers to a position on the bottom endwall. The blade surface coordinate, s in Fig. 2(a) originates at the leading edge stagnation point and is positive on the pressure-side.

The five-hole pressure probe has a diamond-tip of diameter of 1.6 mm and scans the planes-1 to 3 along the (Y, Z) locations on a motorized two-axis traverse controlled by a Velmex^{TM} motor controller. The probe is connected to five differential pressure transducers. The slot length during the probe traverse is masked with a plastic liner to minimize any flow leakage. The unused slots are then covered with tapes to prevent any air leaks. The output voltage-signals from all the pressure transducers are recorded through a National Instrument^{TM} data acquisition

system. The system measures the voltages at a frequency of 100 Hz for 2 seconds from each transducer. The signals are then time-averaged and converted into the pressure unit after applying the appropriate calibration curves. An in-house built LabVIEW^{TM} program both records the pressure signals and controls the motorized traverse. The details of the five-hole probe construction, calibration, and data reduction are provided in [22, 23]. The local velocity components (u, v, w), total pressure, static pressure, and pitch-yaw flow angles are obtained simultaneously from the measurements with the five-hole probe in comparisons to the hot-wire anemometer and other optical probes measuring the velocity field and turbulence properties.

3. Film-cooling Design and Configuration

The location and configuration of the upstream film-cooling slots are shown in Fig. 2(a). Four individual slots in the bottom endwall are placed along the blade-pitch at $0.079C_{ax}$ upstream of the blade leading edge. As shown in Fig. 2(a), two of the slots (82 mm in length) are located upstream of the blade leading edge while the other two are located at the pitchwise middle position of the passage at a 25 mm spacing from each other. The length of the leading edge slot is 82 mm and the middle slot is 55 mm. Figure 2(b) provides the details of the slot geometry in the endwall. The slots are inclined at 30° and the film-flow is delivered in parallel to the cascade inlet flow. Two cases of the film-cooling configurations are investigated by closing off the leading edge slots (82 mm). Thus, the film-cooling case-1 refers to all the slots open while the film-cooling case-2 uses only the two middle slots open (82 mm slots closed). The baseline measurements are obtained without any film-cooling flow. Table 3 provides the film-cooling configurations, the inlet blowing ratios, and the corresponding film-flow mass fractions (MFR) employed for the two film-cooling cases. The mass fraction of the coolant flow, MFR is obtained from the ratio of the total film-flow rate through the two or four slots to the average flow rate in the passage between two adjacent blades. The passage flow rate is computed based on the passage area at inlet and inlet reference velocity. The film-cooling slots are covered with tapes during the baseline measurements.

4. Uncertainty Estimates

The uncertainties in the measured data are estimated based on the 95% confidence interval and in the calculated values are based on the propagation of errors from the measured data as described in [24, 25]. The uncertainty in the reference velocity and pressure is 1.6% and 3.6%, respectively. The maximum uncertainty in the total pressure and total pressure loss coefficient is 7% and 8.2%, respectively. The calculated pitch and yaw angles have the maximum uncertainty of 4% and 5%, respectively. The maximum uncertainty in the film-cooling flow rate is 0.7% and the inlet blowing ratio is 1.4%.

5. Discussions of Results

The flow measurements in the planes-1 to 3 (refer to Fig. 2) cover the spatial area between the bottom endwall and mid-span height in the passage. The time-averaged results are then normalized using the reference properties in Table 2 and presented for the inlet blowing ratios, M_{in} = 1.1-2.3 at a constant inlet Reynolds number, Re = 2.0E+05. The temperature and density ratio of the film-flow to the main flow in the cascade are 1.0 for the results. The "Baseline" case in the results refers to the measurements obtained without any film flow as mentioned earlier. Some qualitative comparisons between the present data and previous work with the coolant leakage are also presented.

Blade surface static pressure coefficient ($C_{P,Blade}$): The static pressure along the blade profile is measured at the mid-span locations ($Y_G/S = 0.5$) of the instrumented blades 3, 4 and 5. The results are presented in Fig. 3 as the static-pressure coefficients, $C_{p,Blade}$ using the Eq. (2). The $C_{p,Blade}$ distributions along the three blade profiles are shown for the Baseline case and along the profile of blade-4 are shown for case-1 and case-2 of the film-cooling. The coordinate s/C=0 in Fig. 3 is located on the stagnation point of blade profile where the $C_{p,Blade}$ is the highest. The values of $C_{p,Blade}$ then decrease along the profile as the flow accelerates. The $C_{p,Blade}$ increases at s/C < -0.33 locations because the flow decelerates from the throat area to the passage exit. The $C_{p,Blade}$ distributions in Fig. 3 for the Baseline case match very closely with each other on the three blade profiles ensuring the flow periodicity and equal mass flow rate in the measurement passages. Also, the $C_{p,Blade}$ distributions for the film-cooling cases match well with the Baseline case to indicate no influence of the film-flow on the blade pressure distributions in the inviscid region. This is desirable for the design loading-conditions on the blade with the endwall film-cooling.

$$C_{P,Blade} = \frac{P_{b,x} - P_{s,r}}{0.5\rho U^2} \tag{2}$$

Normalised axial vorticity ($\omega_x C/U$): The axial vorticity, ω_x computed from the measured pitchwise velocity (v) and spanwise velocity (w) components provides the location and rotational direction of the secondary flows. Because of the complex three-dimensional structure and orientation of the passage vortex system [1, 4], the size and strength of the vortex cannot be fully realized by the ω_x component in the planes-1 to 3 in the present investigation. Figures 4(a)-4(c) compare the contours of normalised axial vorticity at the plane-1 for the Baseline and film-cooling cases at M_{in} = 1.8. The local coordinate Z/P = 0 indicates the location of the suction side of blade 4 in the figures. The data are shown near the endwall region only for clarity of the secondary flows. The circular

contours of high negative values of $\omega_x C/U$ in Fig. 4(a) near the suction (SS) side ($Z/P < 0.1$) indicate the suction side-leg vortex in the Baseline passage. The high positive $\omega_x C/U$ values at $Z/P > 0.1$ in Fig. 4(a) are caused by the boundary layer and pressure side-leg vortex. The strong influences of the film-flow from the slots on the secondary flows and endwall boundary layer are then clearly evidenced in the different $\omega_x C/U$ contours in Figs. 4(b) and 4(c). The $\omega_x C/U$ contours in $Z/P < 0.1$ in Fig. 4(b) are caused as the film-jet from the leading edge slot interacts with and relocates the suction side-leg vortex. The $\omega_x C/U$ contours in $Z/P > 0.1$ in Fig. 4(b) are caused as the film-jet interacts with the boundary layer and pressure side-leg vortex. In the absence of the film-jet from the leading edge, the interactions between film-jet from the two central slots and the suction side-leg vortex are weak in plane-1. The $\omega_x C/U$ contours in $Z/P < 0.1$ in Figs. 4(a) and 4(c) are about the same. The $\omega_x C/U$ contours in $Z/P > 0.1$ in Fig. 4(c), however, show the interactions among the film-jet, boundary layer, and pressure side-leg vortex remain strong. Note that the contours of Figs. 4(b) and 4(c) do not individually identify the film-jet and indicate if the film-jet has weakened the endwall secondary flows due to the complex structures and orientations of the pressure and suction side-leg vortex. The total pressure loss distributions at the exit plane shown later will indicate the influences of film-cooling flow on the strength and size of the passage vortex system.

The endwall region vorticity distributions in plane-2 are shown by the $\omega_x C/U$ contours in Figs. 5(a) to 5(c) for the Baseline case ($M_{in} = 0$) and two film-cooling cases at $M_{in} = 1.8$. The locations of blade pressure side (PS) and suction side (SS) are indicated in Fig. 5. The edge of the passage throat region is located on the SS ($Z/P = 0.0$) in plane-2. As shown by [1, 3, 4], the pressure and suction side-leg vortex are located near the suction side at the axial location of plane-2. The high contour values of $\omega_x C/U$ for the Baseline at $Z/P < 0.3$ in Fig. 5(a) then represent the pressure and suction side-leg vortex. As the film-cooling flow is introduced, the film-jet travels along the passage, interacts with the endwall secondary flows and boundary layer, and changes values and distributions of the $\omega_x C/U$ contours as evidenced in Figs. 5(b) and 5(c). The $\omega_x C/U$ contours for the pressure and suction side-leg vortex are not clearly distinguishable in Figs. 5(b) and 5(c) because of the interactions changing the vortex structures. However, the structures of the passage vortex system must still exist because of the momentum conservation. The changes of the $\omega_x C/U$ contours along the entire pitch in Figs. 5(b) and 5(c) indicate the film coverage over the entire endwall pitchwise at plane-2 location for both the film cooling cases. The full coverage of endwall film-cooling is a desirable result for the high values of the adiabatic film-cooling effectiveness. Comparing the data between Fig. 5(b) and Fig. 5(c) in the location $Z/P < 0.1$, more and stronger film-flow is evident for the film-cooling case-1 than for the case-2 because of the jet from the leading edge slot. The film-jet ejected from the leading edge slot on the pressure side of the passage convects towards the suction side as it travels

along the passage due to the pitchwise pressure gradient [9, 18]. The presence of some additional $\omega_x C/U$ contours about Z/P = 0.2 in Fig. 5(b) compared to those in Fig. 5(c) also indicate the more film coverage by the film-cooling case-1.

The effects of film coverage on the endwall region are further compared by the $\omega_x C/U$ distributions between the film-cooling case-1 and case-2 at M_{in} = 2.3 in plane-2 in Fig. 6. As indicated in the figure, the effects of the film-jet are also evident along the entire pitch (SS to PS) by the changes in $\omega_x C/U$ values compared to those in Fig. 5(a). Because of the higher blowing ratio and mass flux in the film-jet, the absolute magnitudes of $\omega_x C/U$ are higher along most of the pitch in Fig. 6 than those in Figs. 5(b) and 5(c). The $\omega_x C/U$ contours in Fig. 6 also spread more spanwise along Y/S indicating more interactions with the boundary layer as the M_{in} increases. For M_{in} = 2.3 also, the film-jet from the leading edge slot in case-1 causes some additional $\omega_x C/U$ contours in Z/P < 0.1 in Fig. 6(a) compared to those in case-2 in Fig. 6(b) and provides better film coverage on the endwall. Note that the data for the film-cooling cases in both Figs. 5 and 6 appear to be skewed towards the pressure side. This is because the local mass-flux is higher towards the pressure side (PS) for the film-cooling cases than for the Baseline as evidenced in the local mass-flux ratio distributions, $(\rho u)/(\rho U)$ along the pitchline in Fig. 7. The data in Fig. 7 are shown for the M_{in} = 2.3 for the film-cooling cases in plane-2.

Yaw angle deviation (ΔYaw): Flow yaw angle near the endwall is responsible for the strong pitchwise crossflow [26, 27] which then contributes to the development of the passage vortex system. The yaw angles relative to the axial direction in the blade passage increase in the endwall boundary layer as the streamlines of low velocity turn towards the suction side to balance the pitchwise pressure gradient with the opposing radial force [27]. Figure 8 presents the yaw angle deviations, ΔYaw near the endwall in plane-2 for the Baseline and film-cooling cases at M_{in} = 1.8. The difference between the mid-span yaw angle at a given pitchwise location (Z/P, Y/S = 0.5) and the local yaw angle at the same pitchwise location (Z/P, Y/S) is used as the ΔYaw in Fig. 8. The high values of ΔYaw for the Baseline in Fig. 8(a) are caused by the pressure and suction side leg vortex, and the boundary layer. The momentum of the film-jet influences the endwall streamlines to turn less towards the suction side (SS) causing the ΔYaw values to be smaller in Figs. 8(b) and 8(c) than those in Fig. 8(a). The ΔYaw values near the SS and PS for the film-cooling case-1 in Fig. 8(b) are different from those for the case-2 in Fig. 8(c) because of the additional film-jet momentum issued from the leading edge slots. As indicated in [18, 26], the lower ΔYaw values of the endwall flows contribute to the weakening of the passage vortex. This is an additional advantage of the effects of the endwall film-cooling with the right configuration of the coolant slots or holes. The

weak passage vortex reduces the total pressure losses in the blade passage as well as the lifting-off of the film-jet from the endwall to enhance the adiabatic film-cooling effectiveness [16, 17]. Figure 9 compares the ΔYaw in plane-3 at the passage exit between the Baseline and two film-cooling cases at M_{in} = 1.8. The trailing edge (TE) is located at Z/P = 0.0 in the figure. The lower ΔYaw values at Y/S < 0.1 in Figs. 9(b) and 9(c) than those in Fig. 9(a) indicate the strong influences of the film-jet momentum on the boundary layer and secondary flows are also present at the cascade exit. The ΔYaw values about Z/P = 0.0 in Figs. 9(b) and 9(c) are caused by the complex interactions of the TE vortex with the passage vortex and film-jet.

The pitchwise-averaged ΔYaw values are compared between the Baseline and film-cooling cases at plane-3 in Fig. 10. The data are shown for M_{in} of 1.8 and 2.3 to present the effects of the blowing ratio in Figs. 10. The pitchwise-averaged $(\Delta Yaw)_{Pitch\text{-}avg}$ at a given Y/S location in the figure is obtained by computing the arithmetic average of the local ΔYaw values along that Y/S. The average ΔYaw values in Figs. 10 are much smaller for the film-cooling cases than for the Baseline in Y/S < 0.2. Also, the $(\Delta Yaw)_{Pitch\text{-}avg}$ values in Y/S < 0.1 are slightly smaller (by 2°) for case-2 than for case-1. The slight differences in the data in Y/S < 0.1 between the film-cooling cases in Fig. 10 are mostly influenced by the ΔYaw values in the TE vortex region. The smaller turnings of the flow streamlines relative to the inviscid region streamlines at the passage exit are beneficial for the endwall film-cooling flow and design blade-loading of following blade row in the turbine.

Total pressure loss coefficient ($C_{pt,loss}$): The secondary vortex structures result in entropy generation and increase the pressure losses along the blade passage [4, 17, 26]. The total pressure loss from the inlet to exit of the blade passage is a measure of the secondary flow losses and quantifies the aerodynamic performance of the passage. The coefficient of total pressure loss, $C_{pt,loss}$ is estimated from the measured $P_{t,x}$ in Eq. (3). The total pressure losses ($P_{t,r}$ - $P_{t,x}$) in the present cascade are obtained in a pitch-plane slightly downstream of the exit. The investigations of [3, 17, 26] indicate the reductions of adverse effects, size, and strength of the passage vortex system directly correspond to the decrease in $C_{pt,loss}$ at the cascade exit. Equation (3) excludes the pressure losses in the film-cooling slots and inlet boundary layer and is also used by [12, 17, 28, 29].

$$C_{pt,loss} = \frac{P_{t,r} - P_{t,x}}{0.5\rho U^2} \tag{3}$$

The distributions of local $C_{pt,loss}$ contours at plane-3 in Fig. 11 compare the total pressure losses between the Baseline and film-cooling cases at M_{in} = 1.8. The higher the $C_{pt,loss}$ value, the higher the total pressure loss ($P_{t,r}$ - $P_{t,x}$). The high values of $C_{pt,loss}$ in the region of 0.0 < Z/P < 0.2 in Fig. 11(a) are caused by the core of the passage

vortex in the Baseline which is now elevated from the endwall. The blade TE is located at Z/P = 0.0 in Fig. 11 as mentioned earlier. The column of high $C_{pt,loss}$ values in -0.2 < Z/P < 0.0 in Fig. 11(a) is then caused by the TE vortices and their interactions with the passage vortex structure. With the film-cooling flow of case-1, the high $C_{pt,loss}$ values in -0.02 < Z/P < 0.09 representing the passage vortex core in Fig. 11(b) are now located closer to the TE vortex region. For the film-cooling case-2 in Fig. 11(c), the passage vortex core is no longer distinguishable because it is now completely located inside TE vortex. Comparing the size and magnitudes of the $C_{pt,loss}$ values in the core of the passage vortex in Fig. 11, it is apparent that the film-cooling reduces the strength and size of the passage vortex. Also, the local $C_{pt,loss}$ distributions in 0.0 < Z/P < 0.12, in general, are smaller for the case-2 of film cooling than for the case-1. The higher $C_{pt,loss}$ values just above endwall in Figs. 11(b) and 11(c) compared to those in Fig. 11(a) are the results of additional vorticities formed by the interactions between the film-jet and boundary layer. Figure 12 presents the effects of higher M_{in} of 2.3 of the two film-cooling cases on the local $C_{pt,loss}$ distributions. Qualitatively the distributions of $C_{pt,loss}$ contours are almost similar for Figs. 11(b) and 12(a), and for Figs. 11(c) and 12(b) indicating small effects of M_{in} on the passage vortex core as the M_{in} increases from 1.8 to 2.3. However, the location of the high $C_{pt,loss}$ values of the passage vortex core in Fig. 12(a) is slightly higher (Y/S ≈ 0.25) than (Y/S ≈ 0.2) in Fig. 11(b). Also, the contours of high losses adjacent to the right corner of endwall in Fig. 12 appear because of higher M_{in} and mass- flux of the film-flow. The presence of the film-jet along the endwall in both Figs. 11 and 12 is desirable for the enhanced film-cooling coverage. In comparisons to the present data, the local gross-loss distributions in the passage vortex regions of [12] are located closer to the mid-span, but away from the TE vortex region and higher in magnitudes with the leakage flow relative to no leakage flow.

Figure 13(a) presents the mass-averaged global total-pressure loss coefficient, $C_{Pt,Loss}$ in the plane-3 as the M_{in} varies. The global $(C_{Pt,Loss})_{mass\text{-}avg}$ at a M_{in} is computed from Eq. (4) integrating over the entire measurement area (Y/S = 0 to 0.5) in plane-3. The Simpson's trapezoidal rule is applied for the numerical integration of Eq. (4) with dA_y determined based on the spatial distance between data points. The mass-averaged loss coefficient for the Baseline is also indicated in the Fig. 13(a). The comparisons in Fig. 13(a) show average $C_{Pt,Loss}$ increases with M_{in} for the case-1. The average $C_{Pt,Loss}$ for the case-2 increases till M_{in} = 1.4, but then decreases as M_{in} increases further. Also, the average $C_{Pt,Loss}$ for case-1 is lower at $M_{in} \leq 1.4$ and higher at $M_{in} > 1.4$ than those for case-2. The spike in the loss distribution at M_{in} = 1.4 for the case-2 is caused primarily by the higher local losses just above the endwall as the film-jet and boundary layer mixes. The higher film-jet momentum at $M_{in} > 1.4$ decreases the near endwall losses to reduce the mass-averaged data for case-2 in Fig. 13(a). Thus, for the objectives of achieving higher film-cooling effectiveness with lower secondary flow losses, the film-cooling case-1 with four coolant slots

may perform better than the case-2 at $M_{in} \leq 1.4$. However, at $M_{in} > 1.4$ the film-cooling case-2 may also provide good aerodynamic performance and film-cooling coverage. Note that the average $C_{Pt,Loss}$ is always lower for both the film-cooling cases than for the Baseline at $1.1 \leq M_{in} \leq 2.3$. In comparisons to the case-1 of film-cooling data in Fig. 13(a), the net mixed-out losses of [12] show similar trend as the coolant flow rate increases and the average $C_{Pt,Loss}$ of [29] is 0.31% smaller for 1% coolant flow than that for the no-coolant flow.

$$\left(C_{Pt,loss}\right)_{mass-avg} = \int_{A_y} \frac{\rho u\left(P_{t,r} - P_{t,x}\right)}{0.5\rho U^2 M} dA_y \tag{4}$$

The compressor supplies the film-cooling flow in the gas turbine. The load on the compressor increases with the blowing ratio. The total pressure loss performance across the turbine passage per unit of the coolant mass flow rate is thus important for the gas turbine loading and operating costs. Figure 13(b) provides the mass-averaged $C_{Pt,Loss}$ at plane-3 per unit of coolant mass fraction (MFR) at different M_{in}. The coolant flow MFR is provided in Table 3 for different M_{in}. The average $C_{Pt,Loss}$ values in Fig. 13(b) are obtained from the data in Fig. 13(a). As shown in Fig. 13(b), the $(C_{Pt,Loss})$/MFR decreases as the M_{in} increases and is always smaller for the film-cooling case-1 than for the case-2. The difference in $(C_{Pt,Loss})$/MFR between the two film-cooling cases, however, decreases at $M_{in} > 1.4$.

6. Summary and Conclusions

The effects of film-cooling on the endwall secondary and boundary layer flows are measured and presented as the film-flow is delivered from the slots in the endwall just upstream of the inlet of a linear vane cascade. The two-dimensional cascade is constructed based on the hub-side geometry and blade profile of the 1st stage nozzle guide vane of the GE-E^3 engine. Four discrete slots inclined at 30° and configured along the entire blade pitch are employed to provide the film-cooling flow at four blowing ratios between 1.1 and 2.3 and at a temperature ratio of 1.0. Measurements are obtained with all four slots open (case-1) and with only two middle slots open (case-2) for the film-cooling flow. The results are compared between the Baseline (no film-cooling) and two film-cooling cases.

The coefficients of pressure along the blade surface indicate the influences of film-flow remain confined near the endwall irrespective of the coolant flow rate. The blade loading can be assumed unaffected when the slot film-cooling is employed which is desirable for any design modifications in the blade passage endwall. The normalized axial vorticity distributions along the endwall indicate the film-jet interacts with the passage-vortex legs and boundary layer and changes their orientations, distributions, and strengths. The film-cooling case-1 with the four

slots delivers more jet on the suction side along the passage than the film-cooling case-2 because of the leading edge slots.

The momentum of the film-jet adds with the boundary layer flow causing the endwall region streamlines to deviate less from the freestream streamlines towards the suction side. Such deviations of the endwall streamlines are further reduced as the blowing ratio or mass-flux of the film-flow increases. The smaller deviations of the endwall streamlines relative to the freestream streamlines help the film-jet travel along the passage and cover the pitchwise distance.

The local distributions of the total pressure losses at the cascade exit are reduced in the region of secondary flow with the film-cooling flow. The total pressure losses are also smaller adjacent to the TE vortex region for the film-cooling case-2 than for the case-1. The film-jet from the leading edge slots in case-1 introduces additional vorticities in the boundary layer region to increase the total pressure losses. The mass-average of the total-pressure losses at the cascade exit show the average losses are always lower with the film-cooling flow than without (Baseline). The overall mass-average losses are also smaller at the small blowing ratios, but higher at the high blowing ratios for the film-cooling case-1 than for the case-2. The mass-averaged pressure losses per unit mass fraction of the film-flow is always lower for the case-1 compared to the case-2 for the blowing ratios tested.

The endwall film-cooling flows are primarily employed to provide the film protection of blade passage endwall from the hot mainstream gas. However, the results from the present investigation indicate the coolant flow also influences the endwall region boundary layer and secondary flows along the passage. The consequences of the affected endwall flows are then reflected back to the film coverage on the endwalll and show up in the aerodynamic losses. The results are beneficial to the understanding of the behaviour and the optimal design of the full coverage film-cooling through the validations of numerical models.

Acknowledgments

The authors are grateful for the financial support of the AMRSCOR program of the South African government. The assistance of Mr. Adeola Shote in obtaining some data is appreciated.

Table 1 Geometric parameters of vane cascade

Scale factor	C_{ax} (m)	C (m)	C/S	C/P	Incidence
6	0.203	0.355	1.479	1.328	0°

Table 2 Reference flow parameters

Freestream velocity, U (m/s)	10.0
$P_{s,r}$ (kPa), (-gage)	60
Boundary layer thickness, δ/S	10 %
Streamwise turbulence intensity	3 %
Air temperature (K)	298
Air density, ρ (kg/m^3)	1.02
Reynolds Number, Re	2.0E+05

Table 3 Film-cooling MFR(%)

M_{in}	Case-1 (4 slots open)	Case-2 (2 middle slots open, 82 mm slots closed)
1.1	0.8	0.72
1.4	2.53	1.6
1.8	5.12	2.4
2.3	8	3.71

References

[1] Wang, H.P., Olson, S.J., Goldstein, R.J., and Eckert, E.R.G., "Flow Visualization in a Linear Turbine Cascade of High Performance Turbine Blades," *Journal of Turbomachinery*, Vol. 119, No. 1, 1997, pp. 1–8.
doi:10.1115/1.2841006

[2] Simon, T.W., and Piggush, J.D., "Turbine Endwall Aerodynamics and Heat Transfer," *Journal of Propulsion and Power*, Vol. 22, No. 2, 2006, pp. 301-312.
doi: 10.2514/1.16344

[3] Mahmood, G.I., Gustafson, R., and Acharya, S., "Experimental Investigation of Flow Structure and Nusselt Number in a Low-Speed Linear Blade Passage with and without Leading-Edge Fillets," *Journal of Heat Transfer*, Vol. 127, No. 5, 2005, pp. 499-512.
doi:10.1115/1.1865218

[4] Ligrani, P., Potts, G., and Fatemi, A., "Endwall Aerodynamic Losses from Turbine Components within Gas Turbine Engines," *Propulsion and Power Research*, published online 23 Jan. 2017, http://www.sciencedirect.com/science/article/pii/S2212540X17300068 [retrieved 16 Feb 2017].
doi: 10.1016/j.jppr.2017.01.006

[5] Thomas, M., and Povey, T., "Improving Turbine Endwall Cooling Uniformity by Controlling Near-Wall Secondary Flows," *Journal of Aerospace Engineering*, Vol. 0, No. 0, 2016, pp. 1-17.
doi: 10.1177/0954410016673092

[6] Friedrichs, S., Hodson, H.P., and Dawes, W.N., "Aerodynamic Aspects of Endwall Film-Cooling," *Journal of Turbomachinery*, Vol. 119, No. 4, 1997, pp. 786-793.
doi: 10.1115/1.2841189

[7] Salvadori, S., Ottanelli, L., Jonsson, M., Ott, P., and Martelli, F., "Investigation of High-Pressure Turbine Endwall Film-Cooling Performance Under Realistic Inlet Conditions," *Journal of Propulsion and Power*, Vol. 28, No. 4, 2012, pp. 799-810.
doi: 10.2514/1.B34365

[8] Bogard, D.G., and Thole, K.A., "Gas Turbine Film Cooling," *Journal of Propulsion and Power*, Vol. 22, No. 2, 2006, pp. 249-270.
doi: 10.2514/1.18034

[9] Mahmood, G.I., Saha, A.K., and Acharya, S., "Secondary Flow and Upstream Film Cooling in a Linear NGV Cascade in Compressible Flows: Computations and Experiments," Heat Transfer, Fluid Mechanics and Thermodynamics (HEFAT), 6th International Conference, Papert MG1, July 2008.

[10] Li, X., Ren, J., and Jiang, H., "Film Cooling Effectiveness Distribution of Cylindrical Hole Injections at Different Locations on a Vane Endwall," *International Journal of Heat and Mass Transfer*, Vol. 90, 2015, pp. 1-14.

doi: 10.1016/j.ijheatmasstransfer.2015.06.026

[11] Li, X., Ren, J., and Jiang, H., "Multi-Row Film Cooling Characteristics on a Vane Endwall," *International Journal of Heat and Mass Transfer*, Vol. 92, 2016, pp. 23-33.

doi: 10.1016/j.ijheatmasstransfer.2016.06.047

[12] Blanco, E.de la R., Hodson, H.P., and Vazquez, R., "Effect of Leakage Flows and the Upstream Platform Geometry on the Endwall Flows of a Turbine Cascade," *Journal of Turbomachinery*, Vol. 131, No. 1, 2009, pp. 0110041-0110049.

doi: 10.1115/1.2950052

[13] Papa, M., Srinivasan, V., Goldstein, R.J., and Gori, F., "Effect of Gap Geometry on the Cooling Effectiveness of the Wheelspace Coolant Injection Upstream of a Row of Rotor," *Heat Transfer Research*, Vol. 41, No. 6, 2010, pp. 651-667.

doi: 10.1615/HeatTransRes.v41.i6.50

[14] Du, K., and Li, J., "Nupmerical Study on the Effects of Slot Injection Configuration and Endwall Alignment Mode on the Film Cooling Performance of Vane Endwall," *International Journal of Heat and Mass Transfer*, Vol. 98, 2016, pp. 768-777.

doi: 10.1016/j.ijheatmasstransfer.2016.02.014

[15] Oke, R., Simon, T., Shih, T., Zhu, B., Lin, Y.L., and Chyu, M., "Measurements Over a Film-Cooled, Contoured Endwall With Various Coolant Injection Rates," American Society of Mechanical Engineers, Paper 2001-GT-0140.

doi: 10.1115/2001-GT-0140

[16] Thole, K.A., and Thrift, A.A., "Influence of Flow Injection Angle on a Leading-Edge Horseshoe Vortex," *International Journal of Heat and Mass Transfer*, Vol. 55, 2012, pp. 4651-4664.

doi: 10.1016/j.ijheatmasstransfer.2012.04.024

[17] Erickson, R. and Simon, T.W., "Effect of of Stator/Rotor Leakage Flow and Axisymmetric Contouring on Endwall Adiabatic Effectiveness and Aerodynamic Losses," *Heat Transfer Research*, Vol. 42, No. 1, 2011, pp. 45-64.

doi: 10.1615/HeatTransRes.v42.i1.50

[18] Aizon, W.G.W., Funazaki, K., and Miura, T., "Purge Flow Effect on Aerodynamics Performance in High Pressure Turbine Cascade," *Journal of Mechanical Science and Technology*, Vol. 27, No. 6, 2013, pp. 1611-1617.

doi: 10.1007/s12206-013-0407-1

[19] Barigozzi, G., Franchini, G., Perdichizzi, A., Maritano, M., and Abram, R., "Purge Flow and Interface Gap Geometry Influenec on the Aero-thermal performance of a Rotor Blade Cascade," *International Journal of Heat and Fluid Flow*, Vol. 44, 2013, pp. 563-575.

doi: 10.1016/j.ijheatfluidflow.2013.08.012

[20] Schuepbach, P., Abhari, R.S., Rose, M.G., and Gier, J., "Influence of Rim-Seal Purge Flow on the Performance of an Endwall-Profiled Axial Turbine," *Journal of Turbomachinery*, Vol. 133, No. 2, 2011, pp. 0210111-02101110.

doi: 10.1115/1.4000578

[21] Timko, L.P., "Energy Efficient Engine High Pressure Turbine Component Test Performance Report," NASA CR-168289, Jan 1984.

[22] Ligrani, P., Singer, B., and Baun, L., "Miniature Five-Hole Pressure Probe for Measurement of Three Mean Velocity Components in Low-Speed Flows," *Journal of Physics E: Scientific Instruments*, Vol. 22, No. 10, 1989, pp. 868-876.

IP Address: 137.215.99.35

[23] Ligrani, P., Singer, B., and Baun, L., "Spatial Resolution and Downwash Velocity Corrections for Multiple-Hole Pressure Probes in Complex Flows," *Experiments in Fluids*, Vol. **7,** No. 6, 1989, pp. 424-426.

[24] Moffat, R.J., "Describing the Uncertainties in Experimental Results," *Experimental Thermal and Fluid Sciences*, Vol. 1, No. 1, 1988, pp. 3-17.

doi: 10.1016/0894-1777(88)90043-X

[25] Beckwith, T.G., Marangoni, R.D., and Lienhard, J.H., *Mechanical Measurements*, Pearson Prentice Hall, New Jersey, Sixth ed., 2007, pp. 42-45, 54-59.

[26] Mahmood, G.I., and Acharya, S., "Experimental Investigation of Secondary Flow Structure in a Blade Passage With and Without Leading Edge Fillets," *Journal of Fluids Engineering*, Vol. 129, No. 3, 2007, pp. 253-262.

doi: 10.1115/1.2427075

[27] Acharya, S., and Mahmood, G.I., "Turbine Blade Aerodynamics," *The Gas Turbine Handbook*, NETL of the US Department of Energy, 2006. Ch. 4.3, pp. 363-388.

[28] Leishman, B.A., and Cumpsty, N.A., "Mechanism of the Interaction of a Ramped Bleed Slot With the Primary Flow," *Journal of Turbomachinery*, Vol. 129, 2007, pp. 669-678.

doi: 10.1115/1.2752193

[29] McLean, C., Camci, C., and Glezer, B., "Mainstream Aerodynamic Effects Due to Wheelspace Coolant Injection in a High-Pressure Turbine Stage: Part I- Aerodynamic Measurements in the Stationary Frame," *Journal of Turbomachinery*, Vol. 123, 2001, pp. 687-696.

doi: 10.1115/1.1401026

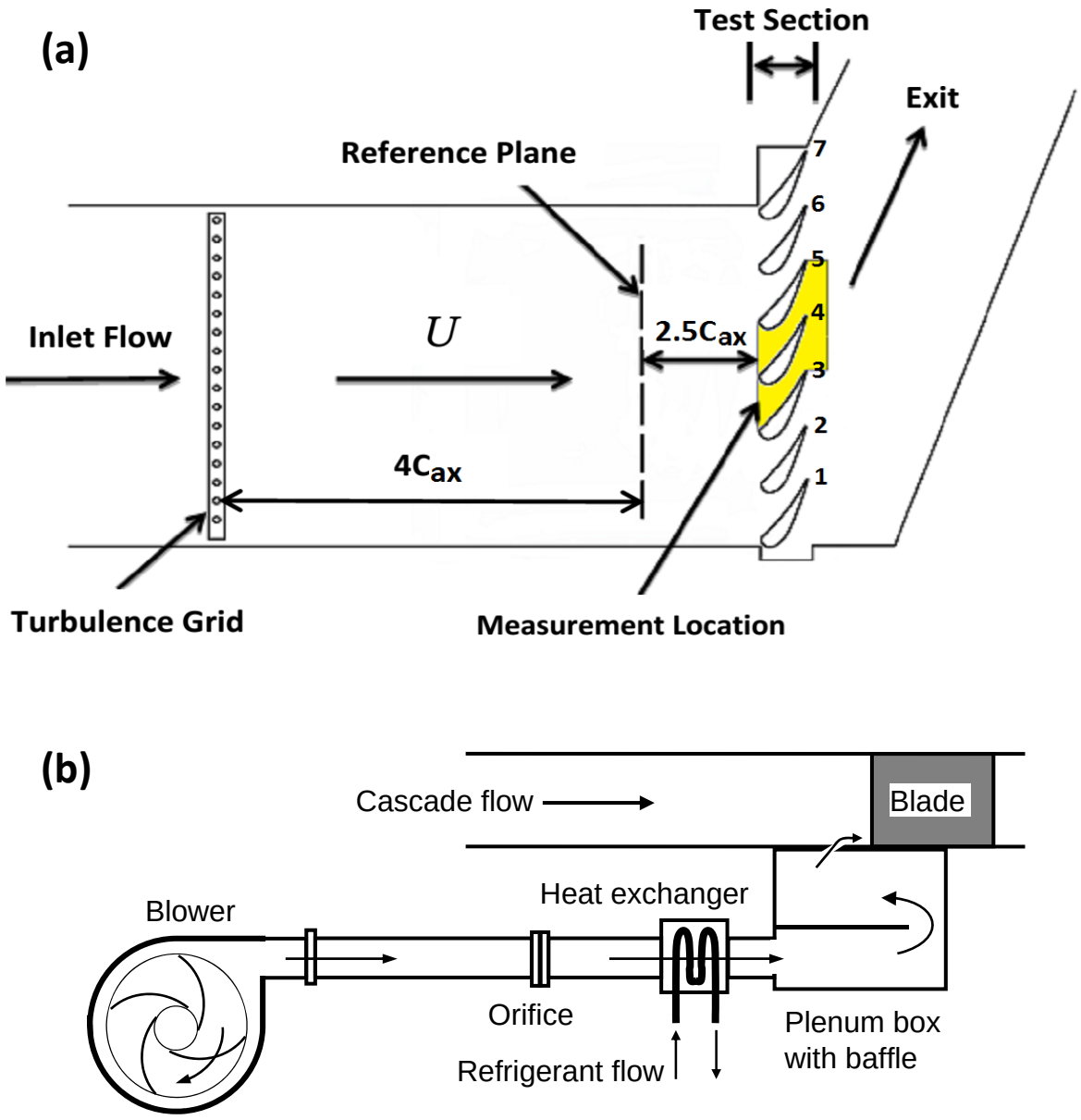

Figure 1: Experimental setup: (a) Wind tunnel and vane cascade; (b) Secondary flow circuit for film-cooling flow.

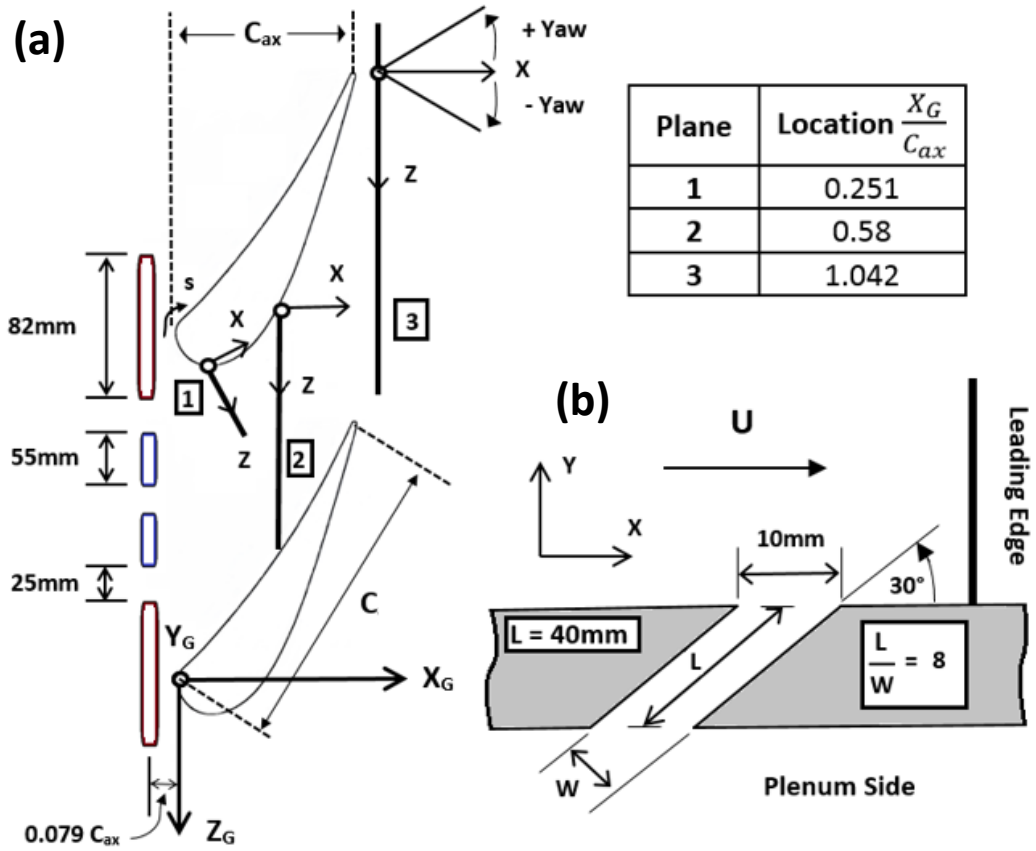

Plane	Location $\frac{X_G}{C_{ax}}$
1	0.251
2	0.58
3	1.042

Figure 2: (a) Coordinate systems and measurement planes with film-cooling slot configuration; (b) Film-cooling slot geometry.

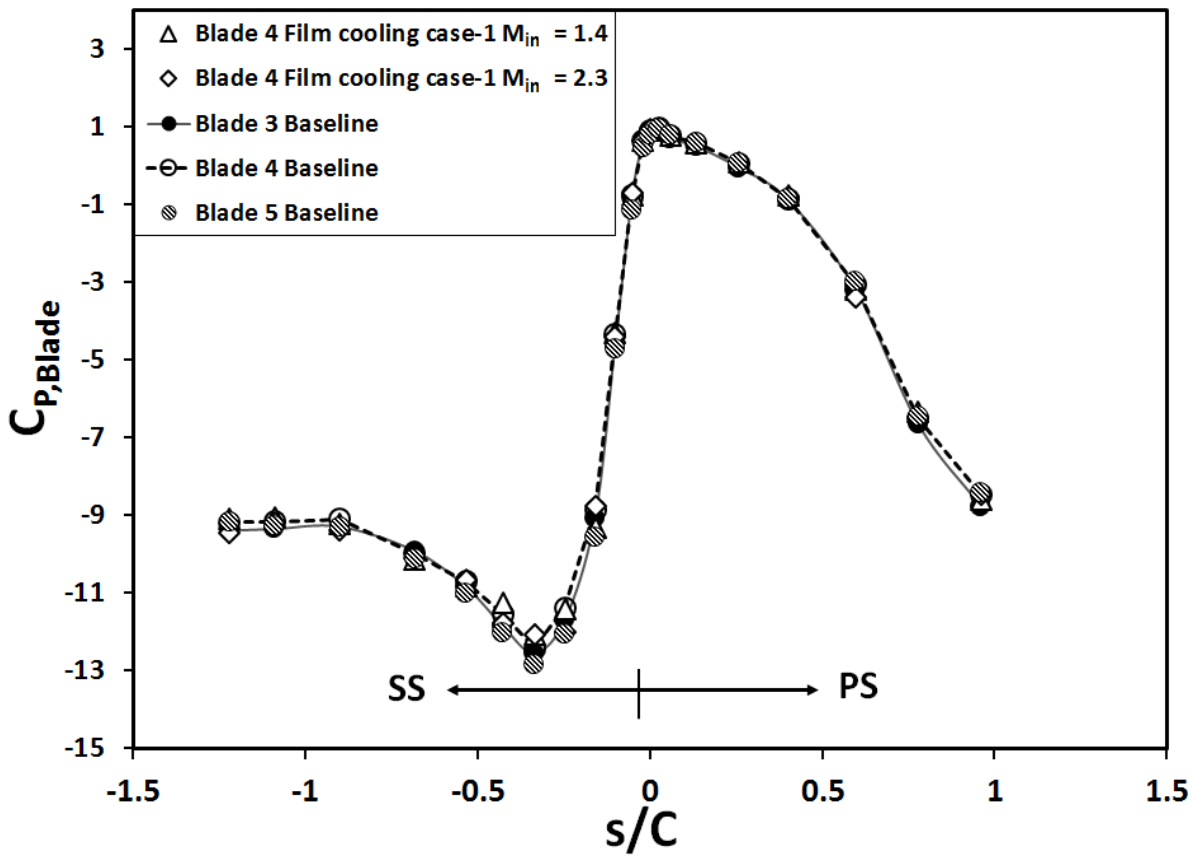

Figure 3: Static pressure coefficients, $C_{P,Blade}$ along blade profile measured on blades 3 to 5 at mid-span ($Y_G/S = 0.5$) location.

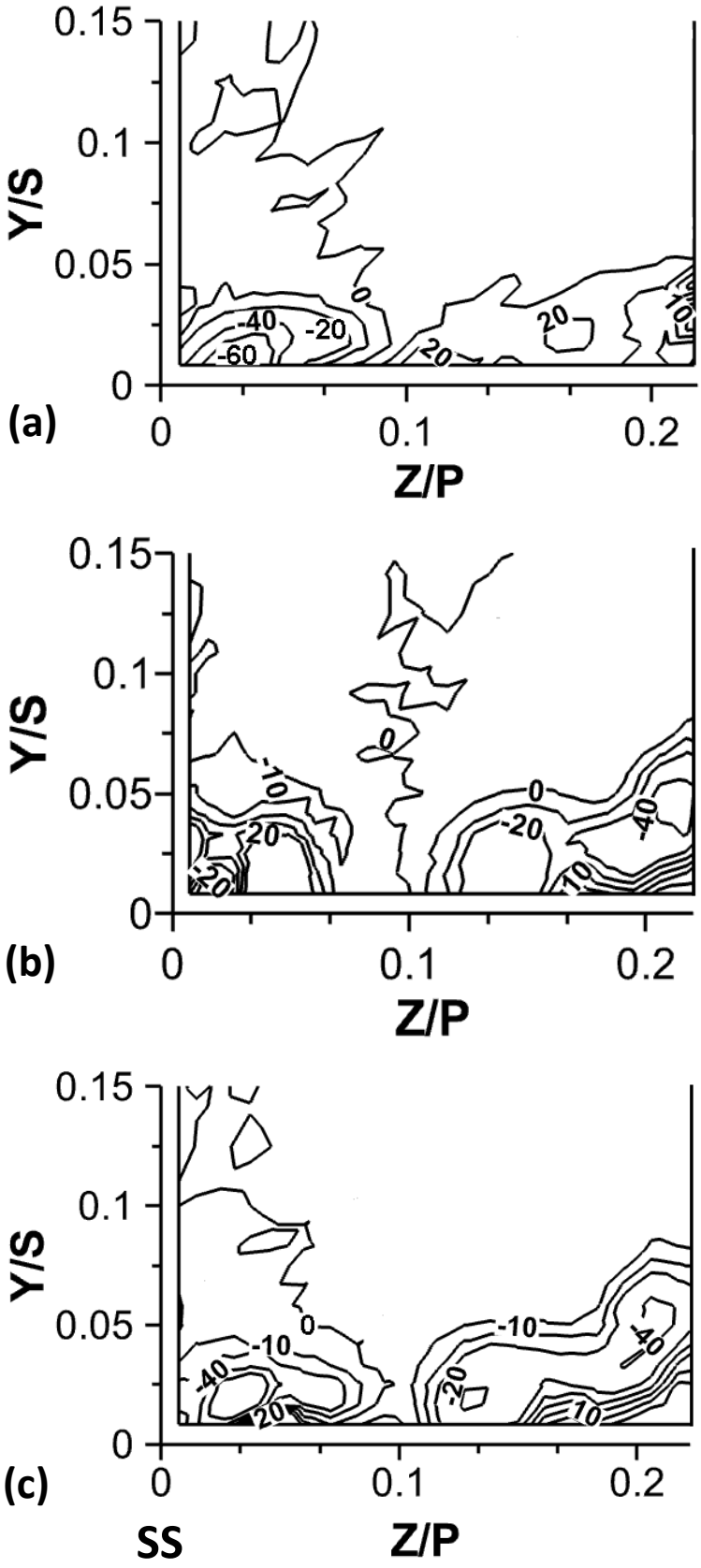

Figure 4: Normalised axial vorticity ($\omega_x C/U$) distributions near endwall in plane-1 for: (a) Baseline; (b) Film-cooling case-1 (M_{in} = 1.8); (c) Film-cooling case-2 (M_{in} = 1.8).

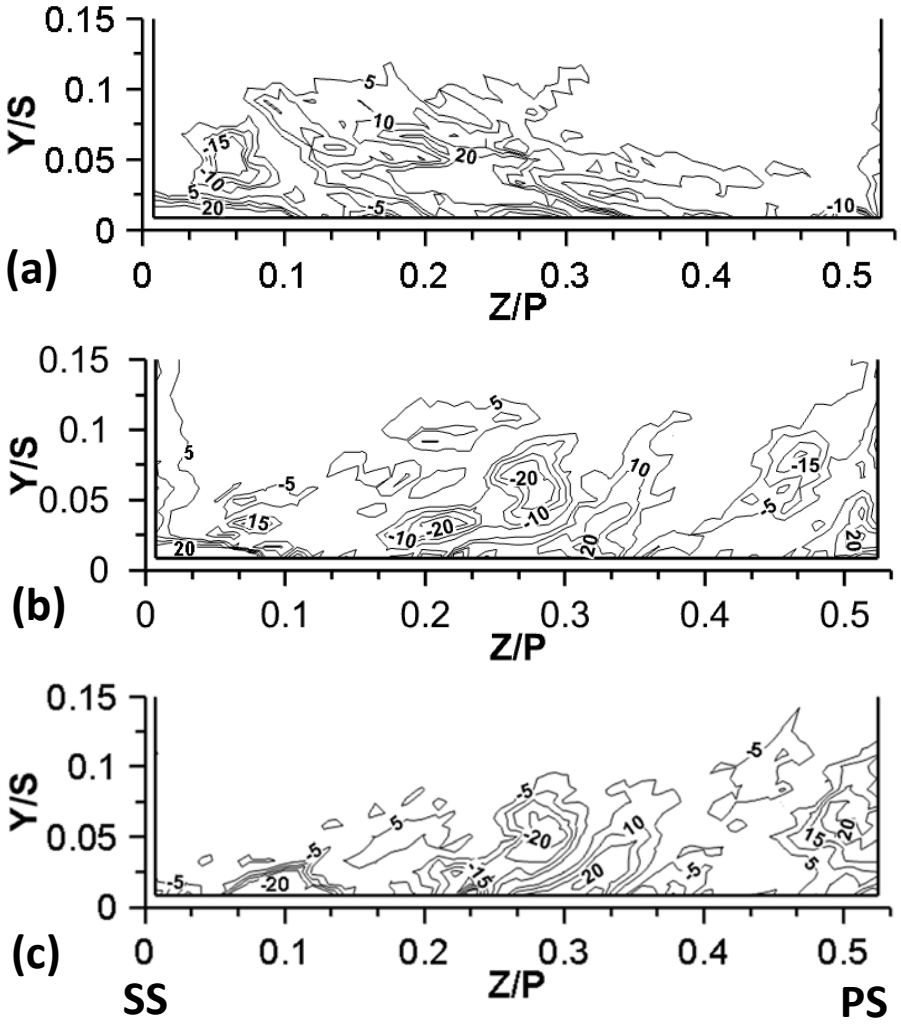

Figure 5: Normalised axial vorticity ($\omega_x C/U$) distributions near endwall in plane-2 for: (a) Baseline; (b) Film-cooling case-1 (M_{in} = 1.8); (c) Film-cooling case-2 (M_{in} = 1.8).

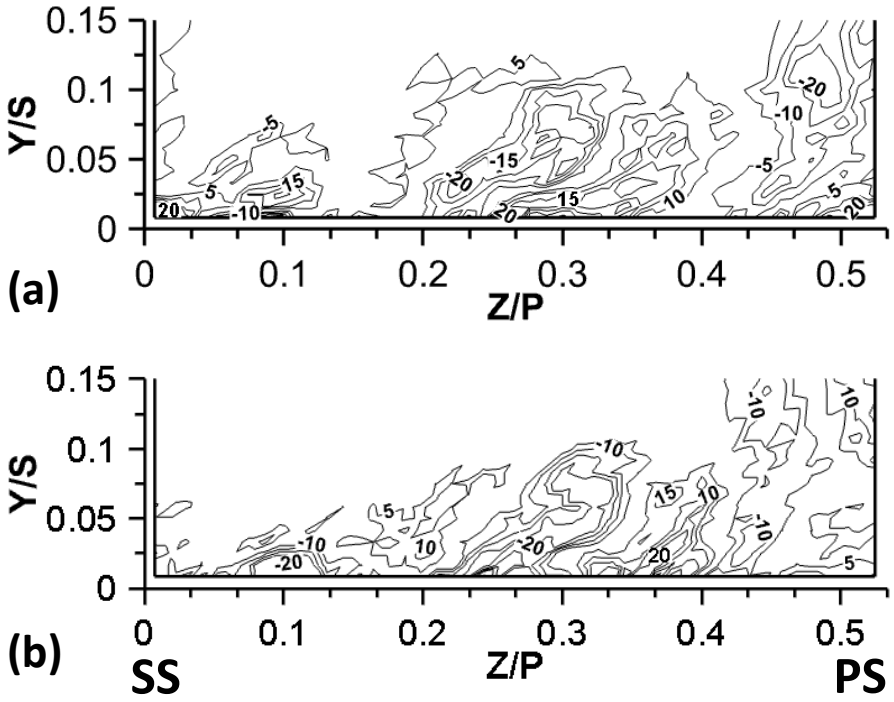

Figure 6: Normalised axial vorticity ($\omega_x C/U$) distributions near endwall in plane-2 for: (a) Film-cooling case-1 (M_{in} = 2.3); (b) Film-cooling case-2 (M_{in} = 2.3).

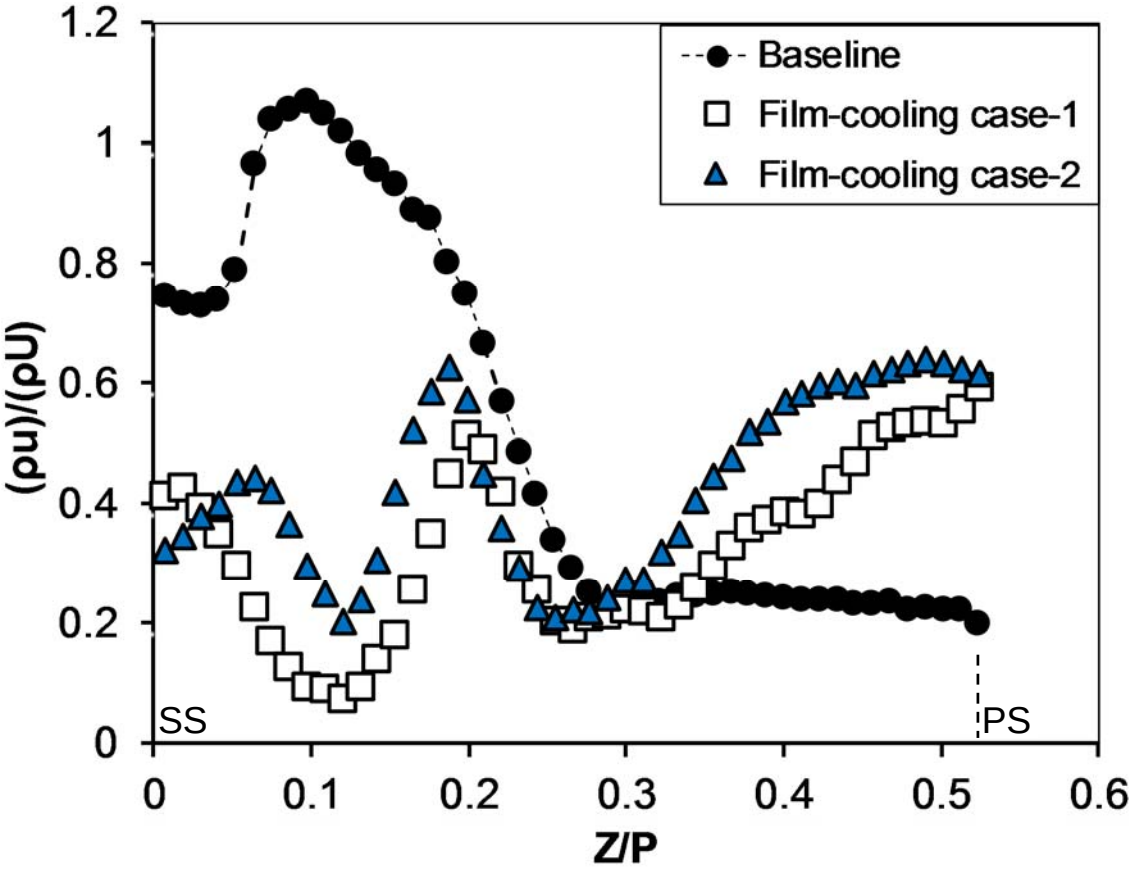

Figure 7: Local mass-flux ratio, (ρu)/(ρU) along pitchline at Y/S = 0.05 in plane-2 for Baseline and two film-cooling cases at M_{in} = 2.3.

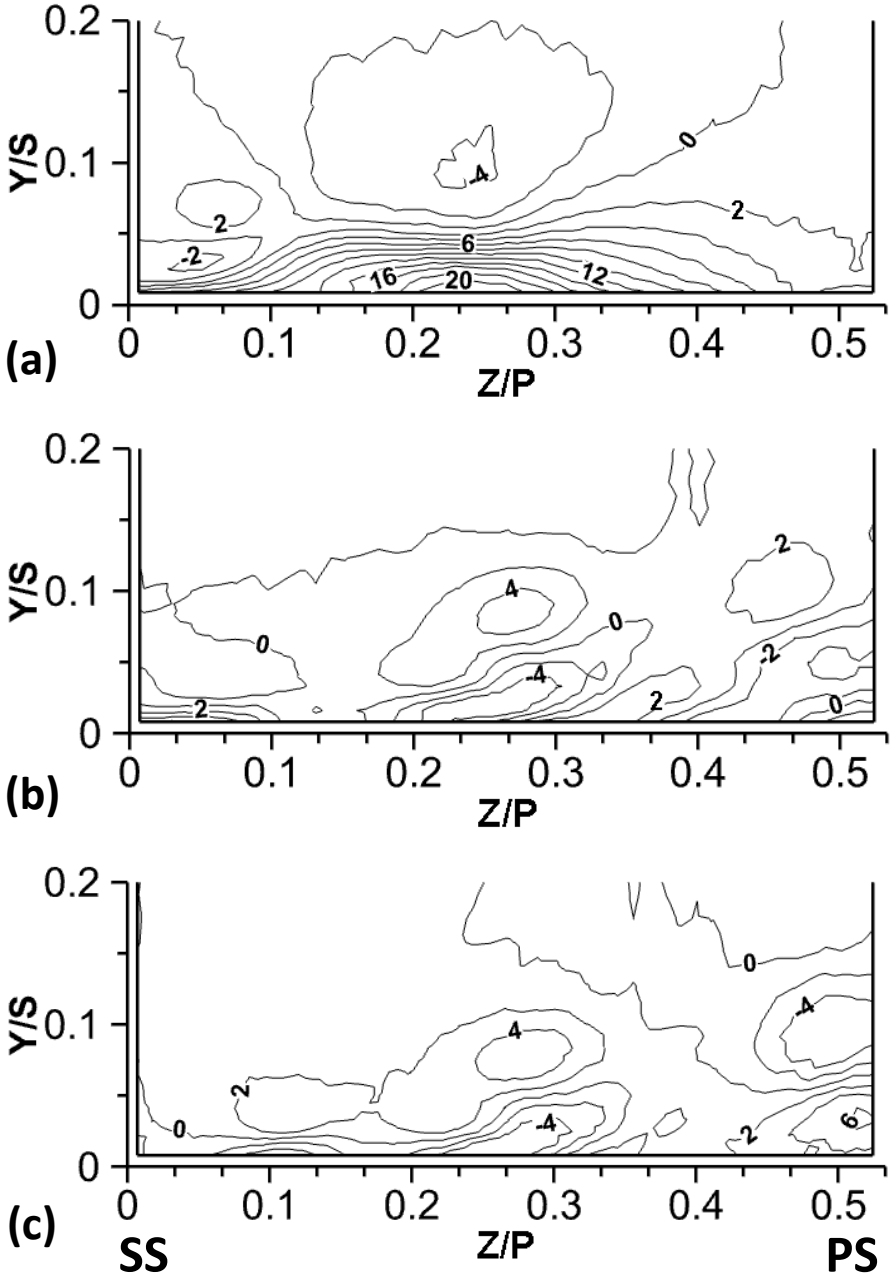

Figure 8: Yaw angle deviations (ΔYaw) in plane-2 for: (a) Baseline; (b) Film-cooling case-1 (M_{in} = 1.8); (c) Film-cooling case-2 (M_{in} = 1.8).

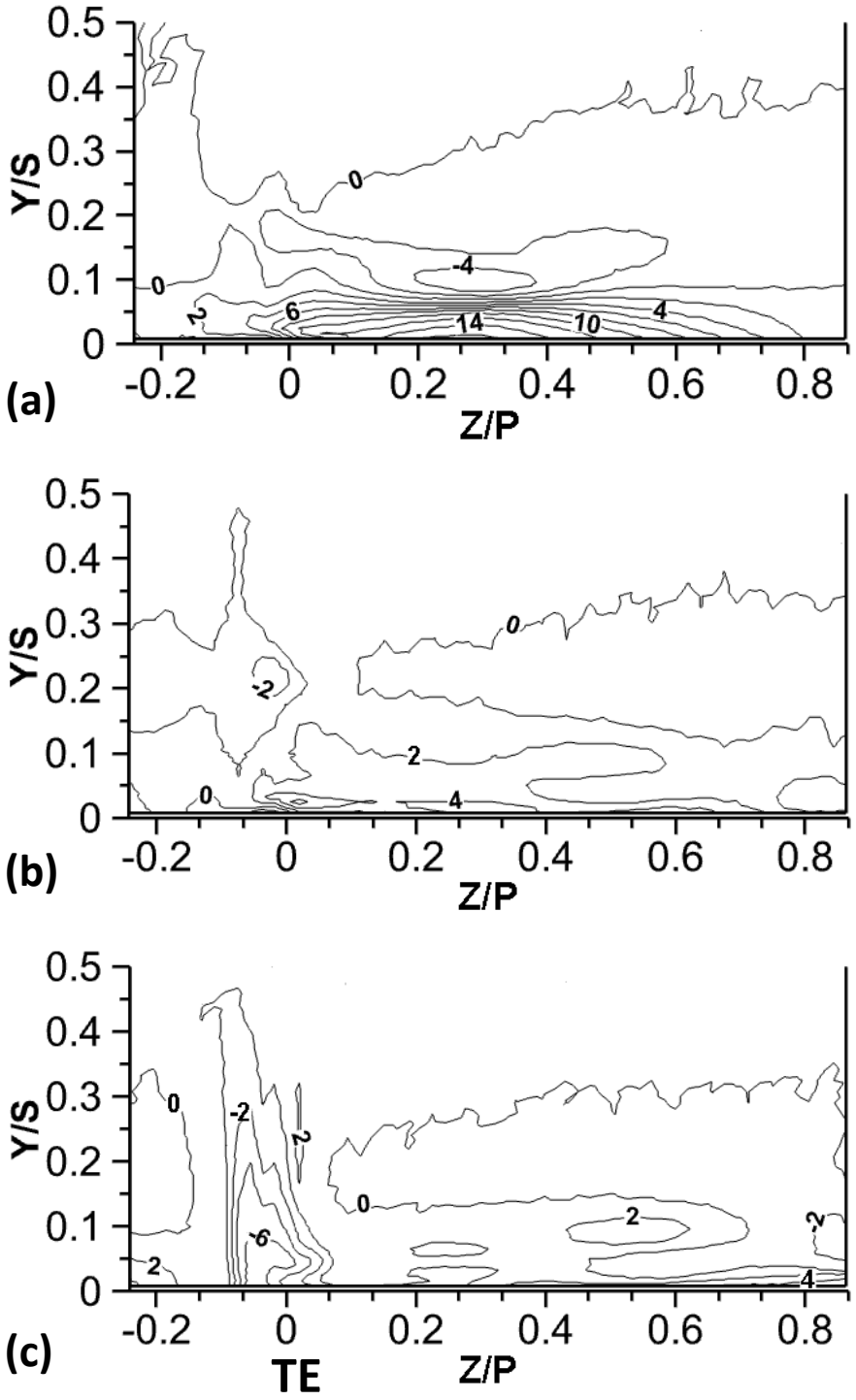

Figure 9: Yaw angle deviations (ΔYaw) in plane-3 for: (a) Baseline; (b) Film-cooling case-1 (M_{in} = 1.8); (c) Film-cooling case-2 (M_{in} = 1.8).

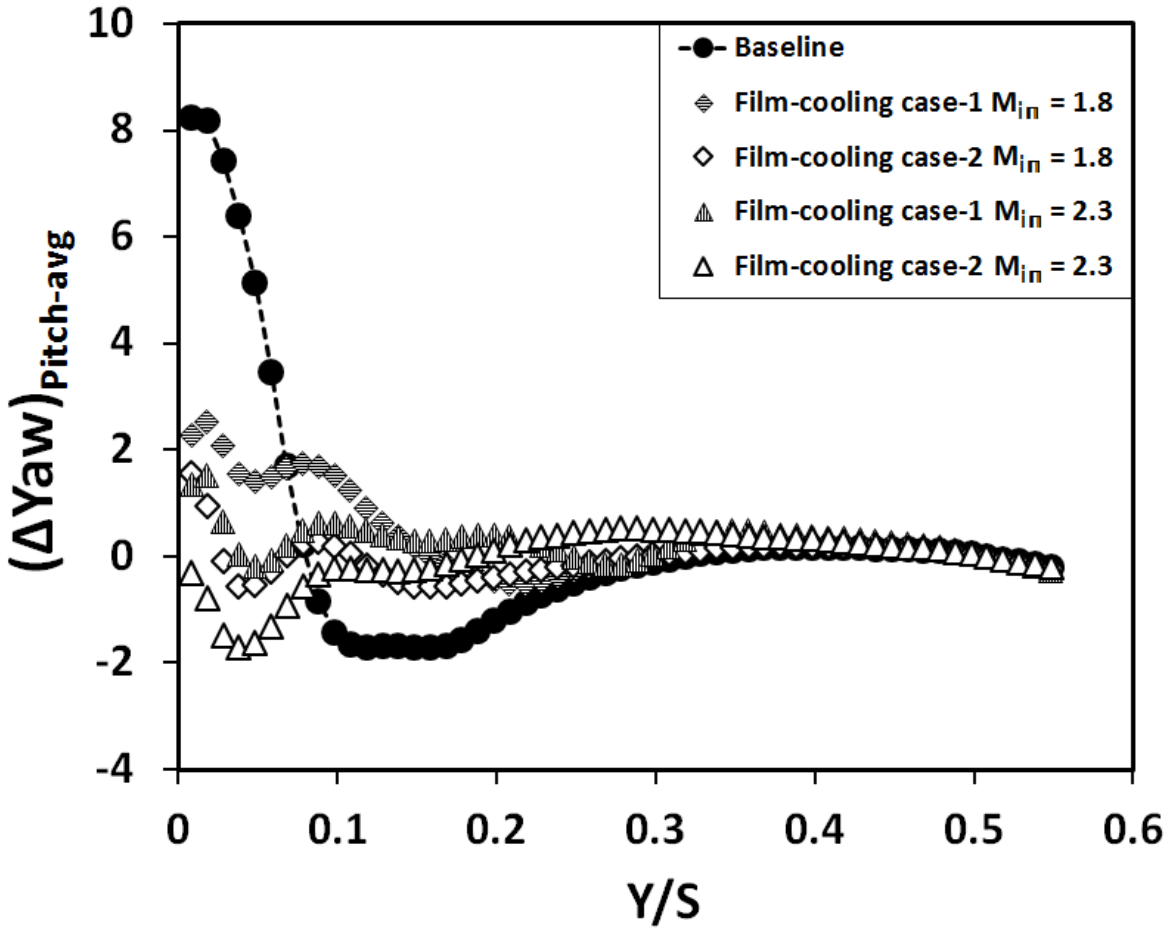

Figure 10: Pitchwise-averaged Yaw angle deviations, $(\Delta Yaw)_{pitch-avg}$ along span in plane-3 for different M_{in}.

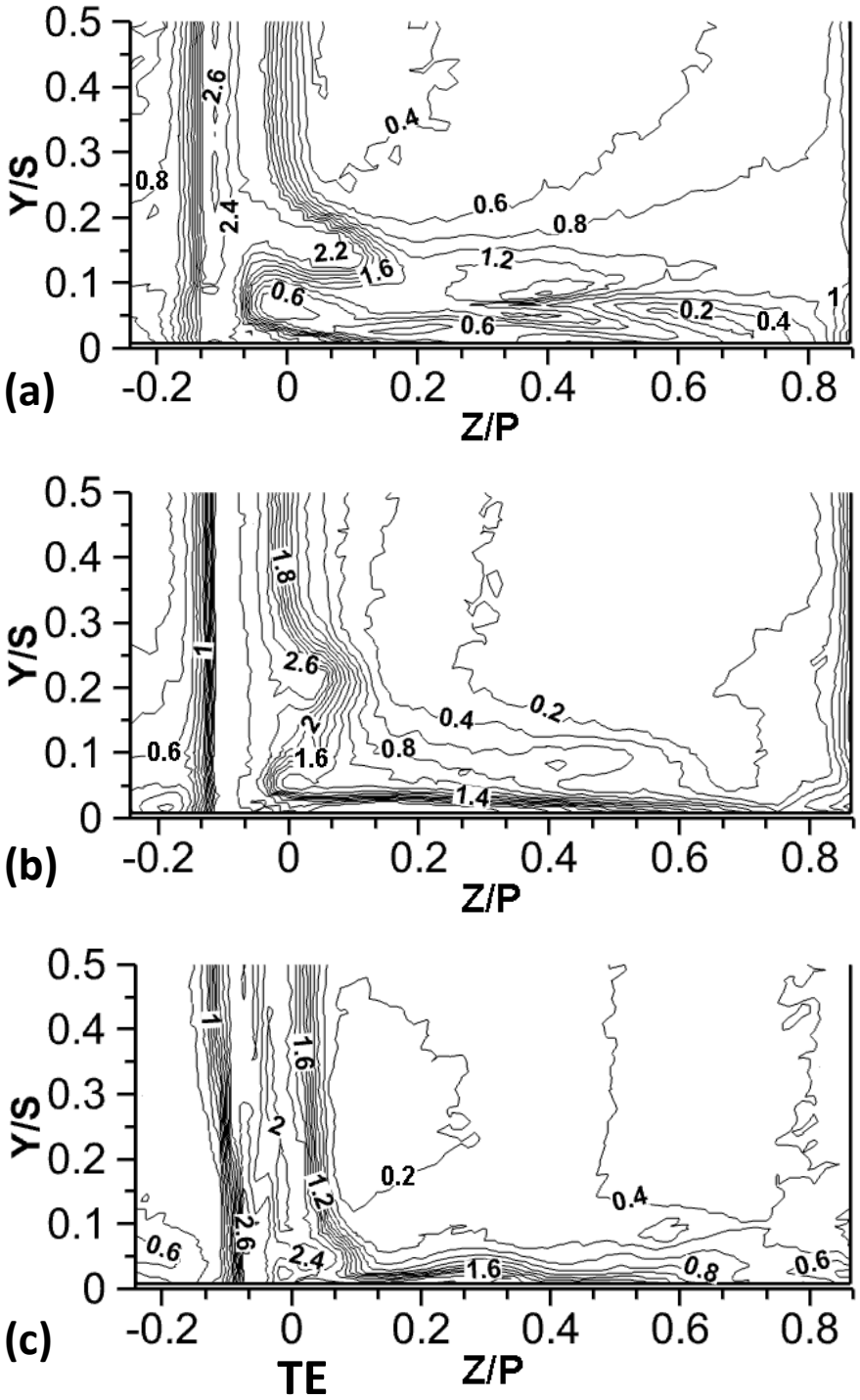

Figure 11: Total pressure loss coefficients, $C_{pt,loss}$ in plane-3 for: (a) Baseline; (b) Film-cooling case-1 (M_{in} = 1.8); (c) Film-cooling case-2 (M_{in} = 1.8).

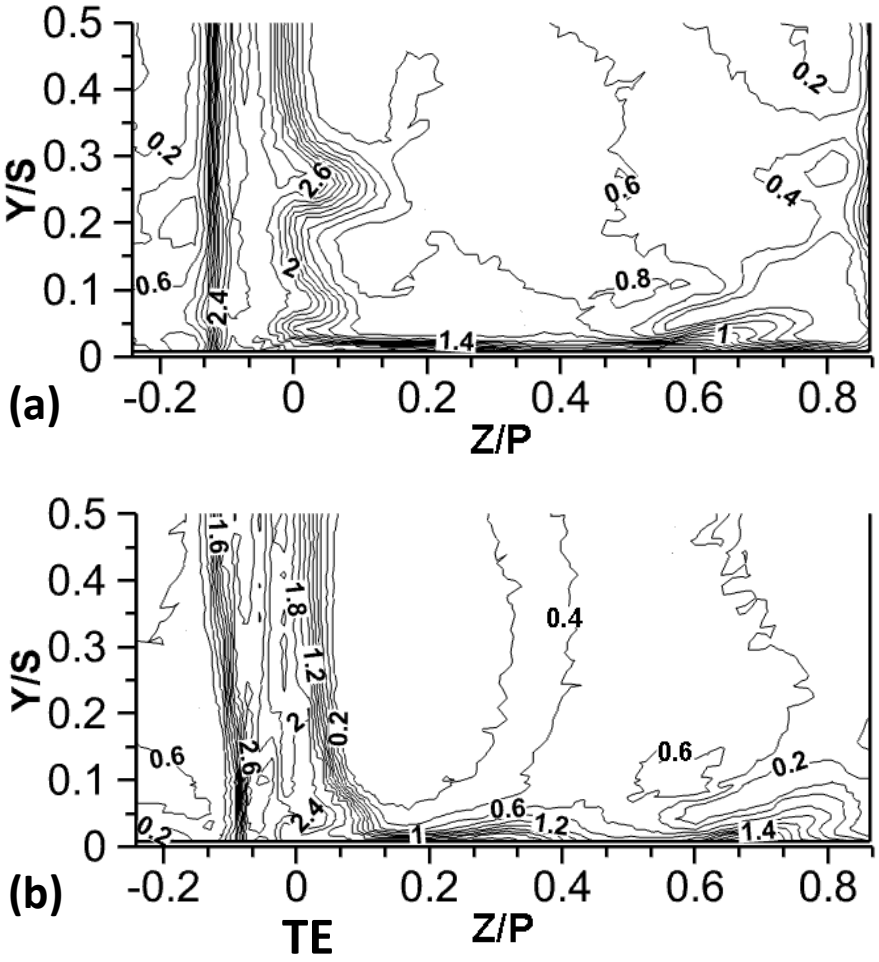

Figure 12: Total pressure loss coefficients, $C_{pt,loss}$ in plane-3 for: (a) Film-cooling case-1 (M_{in} = 2.3); (b) Film-cooling case-2 (M_{in} = 2.3).

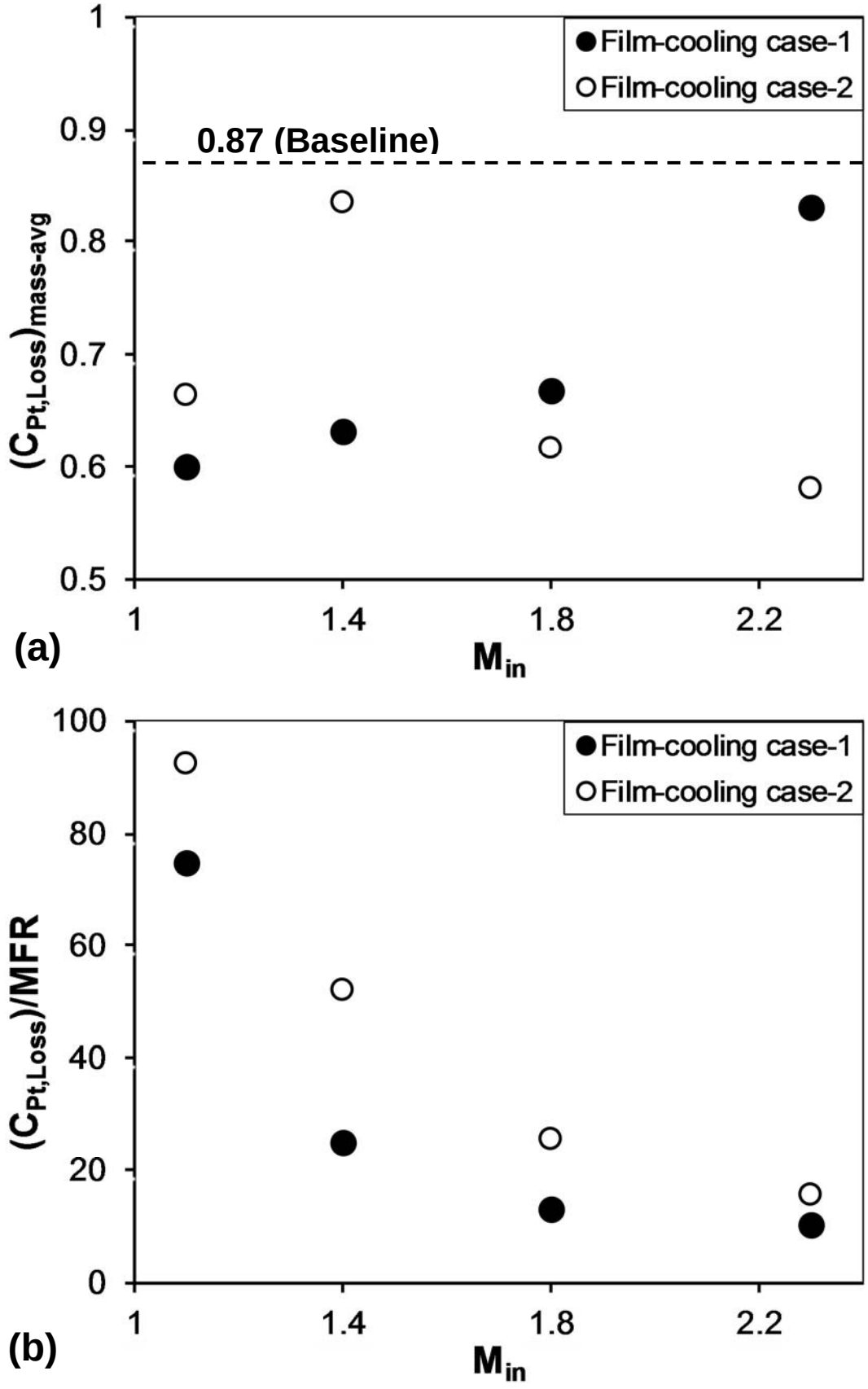

Figure 13: (a) Mass-averaged global $(C_{Pt,Loss})_{mass-avg}$ and (b) Mass-averaged global $C_{Pt,Loss}$ per mass fraction ratio (MFR) of film flow for different M_{in} in plane-3.